



OPEN

Ultra-Small, High-Frequency, and Substrate-Immune Microtube Inductors Transformed from 2D to 3D

SUBJECT AREAS:

ELECTRICAL AND
ELECTRONIC
ENGINEERING

ELECTRONIC DEVICES

Xin Yu, Wen Huang, Moyang Li, Thomas M. Comberiate, Songbin Gong, Jose E. Schutt-Aine & Xiuling Li

Received
15 December 2014Accepted
10 March 2015Published
1 April 2015Correspondence and
requests for materials
should be addressed to
X.L. (xiuling@illinois.
edu)

Department of Electrical and Computer Engineering, Micro and Nanotechnology Laboratory, University of Illinois, Urbana, IL 61801.

Monolithic on-chip inductors are key passive devices in radio frequency integrated circuits (RFIC). Currently, 70–80% of the on-wafer area of most RFIC chips is occupied by the sprawling planar spiral inductors, and its operation frequency is limited to a few GHz. With continuous scaling of the transistor technology, miniaturization and high frequency operation of inductors have become the bottleneck to meet future demands of wireless communication systems. Here we report on-chip self-rolled-up 3D microtube inductors with extremely small footprint, unprecedented high frequency performance and weak dependence on substrate conductivity. The serpentine metal strips are deposited on an oppositely strained silicon nitrides (SiN_x) bilayer. After releasing from the sacrificial layer underneath, the metal/ SiN_x layer is scrolled into a 3D hollow tubular structure by the strain induced unidirectional self-rolled-up technology. Compared to the planar spiral inductors with similar inductances and quality (Q) factors, the footprint of tube inductors is reduced by as much as two orders of magnitude, the frequency at peak Q factor improves more than 5 times. The self-rolled-up 3D nanotechnology platform employed here, that “processes in 2D but functions in 3D”, is positioned to serve as a global solution for extreme RFIC miniaturization with improved performance.

With continuous innovations on transistors and interconnect architectures, complementary metal-oxide-semiconductor (CMOS) technology has been aggressively scaled beyond the soon to be in production 14 nm node, allowing more and more transistors to be integrated on a chip. On the other hand, the progress of miniaturization of passive lumped devices has been severely behind, especially for inductors, the key component in radio frequency integrated circuits (RFICs)^{1,2}. Metal conductors in planar spiral coil structures of the top interconnection layout, due to its compatibility with standard two-dimensional (2D) CMOS processing, are the commonly adopted. In order to achieve required inductance values, more and/or larger turns thus large footprint are often unavoidable due to weak coupling between the spiral wires. Furthermore, crosstalk between the radiated electromagnetic (EM) field and the substrate dramatically limits the inductor maximum working frequency and quality (Q) factor, especially when the substrate is heavily doped. Over the past several decades, significant progress has been made implementing advanced micro-electromechanical systems (MEMS) fabrication technologies to reduce the parasitic effects from the substrates^{3–7} and to scale down the dimension of planar spiral inductors^{8–10}. These improvements include suspending or resistively isolating the spiral wires from the substrates or stacking vertically. However, the intrinsic problems of two-dimensional (2D) or quasi- three-dimensional (3D) open-ended structures inevitably lead to the tradeoff of the on-chip footprint and overall inductor electrical performances. In order to enhance the magnetic induction and reduce the substrate parasitic effects, the true 3D structures that can better confine the magnetic field and reduce large energy dissipation to free space and substrates are much more desirable. However, if conventional fabrication technologies (i.e. planar processing) are used to process 3D structures, issues such as mechanical stability, conformity, alignment, as well as cost, are difficult to address.

In this report, we experimentally demonstrate a type of 3D tube inductor that is extremely small and with unprecedented high frequency performance and weak dependence on substrate conductivity. The 3D spiral tube inductor structure is enabled by the strain-induced Self-Rolled-Up Membrane (S-RUM) technology^{11–19}, where strained thin film nanomembranes spontaneously roll up when released from their mechanical support. This is achieved by the removal of a sacrificial layer underneath the strained membrane, which triggers a net momentum to initiate and maintain the rolling as the embedded opposing biaxial strain is released. The resulted rolled-up



structure is almost a perfectly round hollow cylinder, the diameter of which is determined by the material's mechanical properties and the thickness of each strained layer^{20–22}. By employing a hierarchical SRUM platform with metal strips patterned in 2D and rolled up in multi-turns by a strained silicon nitride (SiN_x) membrane²³, combined with the novel unidirectional rolling process (see supplementary information for details), extremely compact 3D on-chip tube inductors are formed.

Results

Figure 1A and B illustrate the concept of multi-turns rolled-up inductors, using oppositely strained SiN_x bilayers as the rolling vehicle for conducting metal strips. Thin metal strips (Fig. 1A) with length L_s and width W_s connected by metal connecting lines with length L_c and width W_c , along with the two feedlines as the input/output ports of RF signals, are deposited and patterned on top of the SiN_x bilayer. Dual-frequency plasma enhanced chemical vapor deposition (PECVD) is used to deposit the SiN_x bilayer, i.e. the low frequency (LF), compressive layer and high frequency (HF), tensile stressed layer. By etching away the germanium (Ge) sacrificial layer, build-in stresses generate a net rolling moment to trigger the self-rolling process of the SiN_x bilayer and the metal strips, forming a multi-turns 3D tubular structure as shown in Fig. 1B. We emphasize

that well-controlled unidirectional rolling is indispensable in order to produce tightly packed multi-turns in the tube inductors. This is realized by a novel sequence of patterning and deposition enabling coherent unidirectional rolling (Materials and Methods), which involves the use of a mesa and appropriate side-wall covering to ensure coherent tearing throughout the dynamic wet etching process (Fig. S1). Once the Ge sacrificial layer is completely removed, the rolling and tearing processing terminates abruptly and the rolled-up tube inductors are left sitting at the mesa edge held by the SiN_x , as shown in Fig. 1B.

Geometrical control of tube inductor can be precisely realized with desired inner diameters and number of coiled turns, by pre-defining the residual stress, thin film thickness, metal pattern length along the rolling path. For all the structures studied in this work, the SiN_x bilayer thickness is 60 nm (30 nm HF + 30 nm LF) and the metal thickness is 100 nm Au/5 nm Ni. As an example, Fig. 1C shows the top view optical image of a four metal strips and fifteen coiled turns (4-strip/15-turn) tube inductor structure before it is rolled-up, where $W_s = 30 \mu\text{m}$, $L_c = 20 \mu\text{m}$, and $W_c = 10 \mu\text{m}$. Fig. 1D and E are the corresponding SEM images showing the top and side views of the device after rolled-up. The inner and outer diameters are 10 and 15 μm , respectively. The on-chip footprint, which we define as the projection area on the substrate, is $200 \times 15 \mu\text{m}^2$, i.e. $3000 \mu\text{m}^2$ or

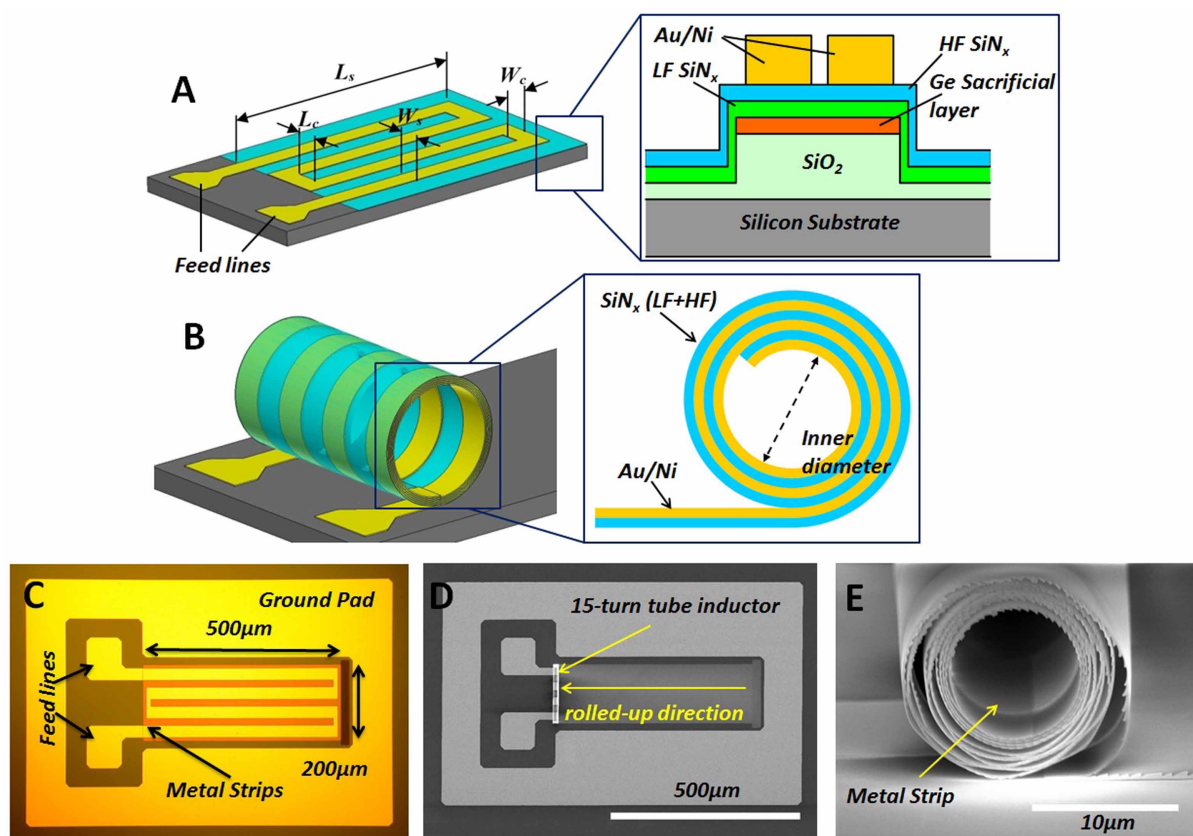


Figure 1 | Schematic illustration of the 3D tube inductor design and images of fabricated devices before and after rolled up. (A) Schematic diagram of the 2D pattern of a tube inductor before rolled-up, with metal strips of width W_s and length L_s connected in series by connecting lines of width W_c and length L_c , and terminated with the feed-lines. The zoomed-in inset shows the cross-sectional structure and material stack. Note that current directions for all turns in the same strip are the same, leading to positive mutual inductance. For adjacent metal strips in the same or different planes, the current directions are opposite, however, the cancelling inductance is negligible when L_c is long enough. (B) The corresponding rolled-up tube inductor. Inset shows the cross-sectional view of the hollow tube where the wall consists of multi-turns of SiN_x bilayer and metal (Au/Ni) strips. (C) Optical image of the before-rolled-up 2D inductor pattern with 4 metal strips ($W_s = 30 \mu\text{m}$ and $L_c = 20 \mu\text{m}$) and RF ground pads and feed-lines. The dimension of the metal strip pattern is $200 \mu\text{m}$ (width) \times $500 \mu\text{m}$ (length) as indicated. (D) SEM image of the 4 metal strips tube inductor with 15 coiled turns, after the metal strip is self-rolled-up along the direction indicated together with the strained SiN_x membrane by the unidirectional rolling technique. (E) Cross-sectional SEM image of the 3D tube inductor with 15 coiled turns. The inner diameter (ID) is $10 \mu\text{m}$ and the outer diameter (OD) is $15 \mu\text{m}$. The scale bar represents $10 \mu\text{m}$.



0.03 mm². Device layouts with other geometrical configurations are also shown in Fig. S2. Naturally, the on-chip footprint grows with the number of, width of, and spacing between the metal strips linearly, and increases only slightly with the number of coiled turns because of the ultra-thin SiN_x wall thickness. Compared to conventional 2D spiral inductors, the rolled-up inductor footprint is drastically reduced, by more than one order of magnitude for similar inductance values.

Discussion

To examine the electrical performance of rolled-up inductors, two port scattering (S) parameters are measured in frequency range from 0.01 to 40 GHz. Parasitic effects of the signal pads are removed by the “open-through” de-embedding procedure (Fig. S3). Measured S_{11} -parameters from samples with different number of coiled turns and metal strips are plotted in the Smith Charts before and after de-embedding (Fig. S4). A lumped single- π equivalent circuit model illustrated in Fig. S5 is used to extract the effective inductance (L) and Q factor from admittance (Y) parameters, which are derived from the de-embedded S parameters.

Fig. 2A and B show the extracted inductances and Q factors as the function of operation frequency for tube inductors with number of coiled turns and metal strips, respectively, on a p -Si substrate ($\rho = 10 \sim 20 \Omega \cdot \text{cm}$). As can be seen, the inductances of all devices hold steady over a wide frequency range before climbing up near f_{Qmax} (the frequency corresponding to the peak Q factor). Just as the planar inductors, Q factors for rolled-up tube inductors increase almost linearly in the low frequency range, then reach the maximum value (Q_{max}), after which they decrease with operation frequency until becomes zero at the self-resonant frequency (f_0). As shown in Fig. 2A, for the 6-strip/15-turn and 6-strip/9-turn devices, the inductance remains at 3.6 and 1.6 nH until f_{Qmax} at 12 and 22 GHz, respectively; for the 6-strip/3-turn device, the inductance remains constant (0.3nH) all the way to millimeter wave band (f_{Qmax} is over 40 GHz, beyond the range of measurement). Compared to the planar spiral inductors with similar inductance values, the operation frequency for tube inductors are much higher than their planar counterparts²⁴. Importantly, the inductance of the 6-strip tube inductor increases from 0.3, 1.6, to 3.6 nH, when the number of turns increases from 3, 9, to 15 turns, respectively, which is much faster than linear increase. Furthermore, in the low frequency range, the slopes of Q factors (the ratio of the effective inductances to direct current resistance) increase with the number of coiled turns. This suggests that, as more turns are formed, the rate of inductance increase is faster than that of resistance. The drop of Q_{max} with increasing number of turns, on the other hand, can be attributed to the fact that more coiled turns correspond to larger inductance and more severe parasitic effects.

Larger inductances can also be achieved by connecting more metal strips in series. As shown in Fig. 2B, for the 15-turn devices, the inductance value is 1.2, 2.4, and 3.6 nH for 2, 4, and 6 metal strips spaced by 20 μm connecting lines, respectively, showing a precise proportional inductance increase with the number of strips. Note that this perfect proportionality observed here only holds truth when metal strips are separated sufficiently far apart that the canceling mutual inductance between strips (with opposite current flow directions) is negligible. In contrast to Fig. 2A, the Q factors, as more metal strips are connected serially with more contact area on the substrate, show nearly identical slopes at low frequency, indicating that the rate of increase of inductance and resistance are almost identical. Also, comparing to the Fig. 2A, Q_{max} and f_{Qmax} do not change much with the number of metal strips, it can be inferred that the parasitic effects from the substrate are weaker than those between coiled turns.

In the Fig. 2C and Fig. S6, the experimental (open symbols) and calculated (solid curves) inductances as functions of the number of coiled turns and metal strips width are plotted with number of metal

strips. The calculated data are derived from our physical model proposed previously²⁵ and details of comparison between experimental and model results are demonstrated in Fig. S7. In the Fig. 2C and S6, excellent agreements between the calculated and experimental inductance values are found in all devices, and the slight discrepancy should be attributed to the additional inductances of connecting lines which are not considered in the model. Physically, the effective inductance of a tube inductor can be comprehended as two parts, the constructive mutual inductance between all coiled turns and the cancelling mutual inductance between adjacent metal strips. Obviously, for a planar straight wire, only self-inductance occurs when RF current flows through it; but once the wire is coiled into a 3D spiral structure with very little gap between each layer, the magnetic flux is expected to be confined into the inner side of hollow low attenuation air core structures. So the constructive mutual inductance between each metal layers become more predominant, owing to the strong EM field coupling. Therefore the tube inductors have much inductance than planar spiral structures with same footprint. As shown in Fig. 2C, the inductance increases exponentially as a function of number of coiled turns, indicating that the mutual inductance is strongly enhanced between turns in the 3D tube inductor structure. This is a result of the close electromagnetic field coupling between turns that have identical current flow directions and are separated only by the 60 nm SiN_x bilayer membrane. On the other hand, different from the macroscopically solenoid inductor, in the tube inductor, the current flowing directions in the two adjacent strips are opposite, which introduces a cancelling mutual inductance between them. Based on our calculation results, when two adjacent strips are spaced (L_c in Fig. S8) far enough, the cancelling inductance can be neglected. In Fig. 2C, the length of connecting line is 20 μm , which has made the cancelling inductance smaller than 1% of inductance for one spiral metal strip with 15 turns. Therefore, when more metal strips are connected in series, the inductance can increase proportionally to the number of strips, providing another way to increase inductance without changing the number of turns.

For an inductor, only the energy stored in the magnetic field is desired, and any energy stored in the electric field induces parasitic resistance and capacitance. In the series branch of the equivalent circuit model of a tube inductor, both ohmic loss (DC range) and skin effect (RF range) should be minimized. Based on DC measurement results, 100 nm thick Au film under our optimized deposition condition has a resistivity that is 1.3 times larger than its bulk value. So, at 40 GHz high frequency, the skin depth is 420 nm. Therefore, the skin effect can be ignored and the Q factor is mainly determined by the ohmic loss from the conduction layer. In the shunt branch, the parasitic capacitances include the crosstalk capacitance (C_c) between adjacent turns and the substrate parasitic capacitance (C_s), which consists of SiO₂ capacitance (C_{ox}) and doped Si capacitance (C_{Si}). In particular, C_c cannot be neglected between turns because of the gap between each turn is only 60 nm thick of SiN_x membrane. As shown in Fig. S9, comparing the open-ended device structure of planar spiral inductors, considerable electromagnetic (EM) field penetrates and dissipates into the substrate. In contrast, the 3D hollow tubular structure of the tube inductor confines most of EM field inside the tube, with little dissipation into the substrate. Therefore the C_s plays a secondary role relative to C_c . Indeed, based on the extracted parameters and calculated results for a $\rho = 10 \sim 20 \Omega \cdot \text{cm}$ p -Si substrate, the overall inter-turns C_c is tens of femto-faradays (fF), and the combined C_{ox} and C_{Si} is only a few fF (Table S1).

In order to comprehensively evaluate the substrate effect, a large set of tube inductor devices with identical material but different geometrical configurations are fabricated on three different kinds of substrates, $\rho = 1 \sim 5 \Omega \cdot \text{cm}$ p -Si and c -plane sapphire, in addition to the $\rho = 10 \sim 20 \Omega \cdot \text{cm}$ p -Si substrate used previously. Plotted in Fig. 2D are the Q_{max} and f_{Qmax} as the function of inductances for the three types substrates. The frequency dependence of inductances and

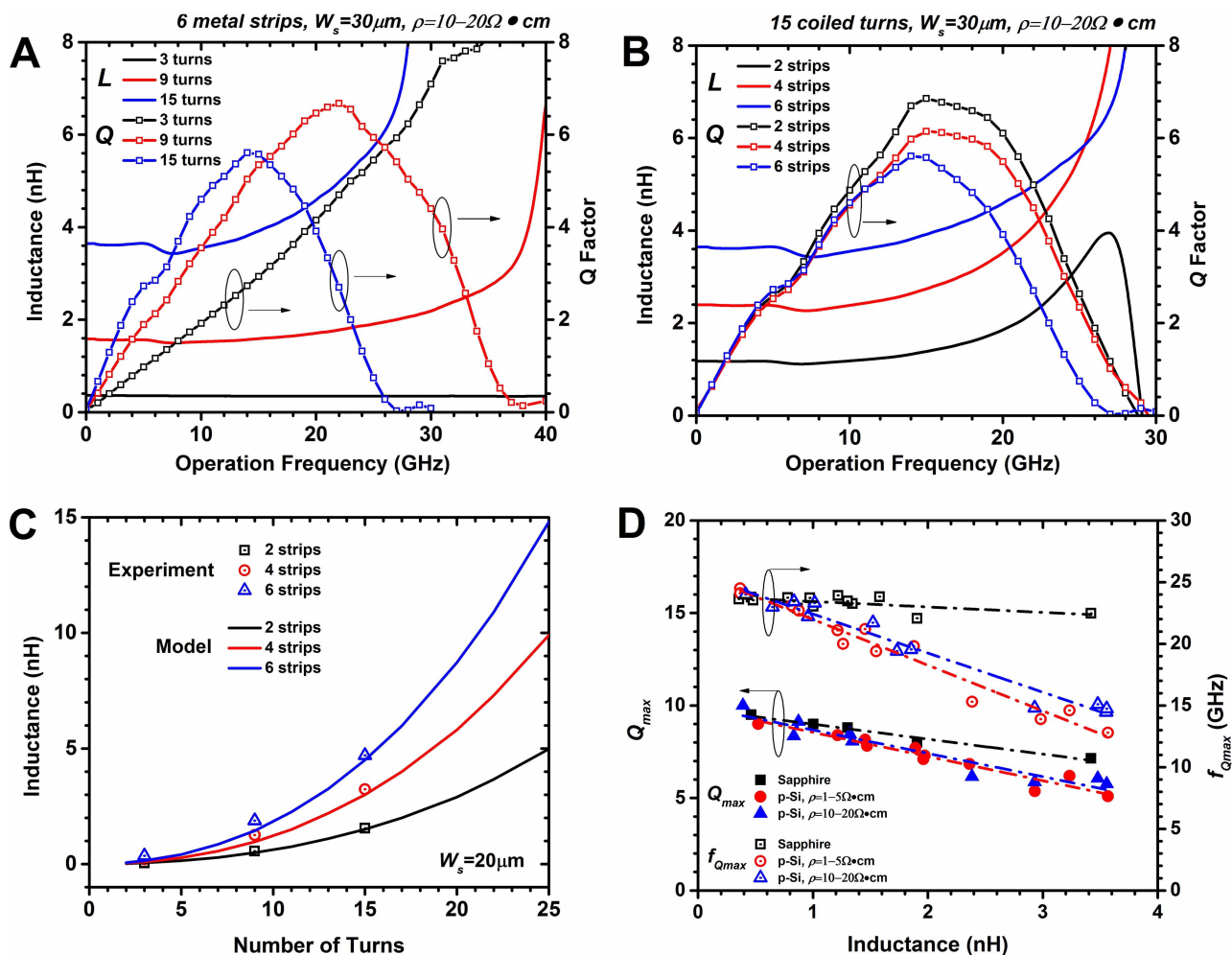


Figure 2 | RF performance of tube inductors and substrate immunity. (A) Measured inductances (solid lines) and Q factors (symbol lines) versus operation frequency for a series of tube inductors with 6 metal strips, $W_s = 30 \mu\text{m}$, but different number (3, 9, and 15) of coiled turns on a $\rho = 10 \sim 20 \Omega\cdot\text{cm}$ p-Si substrate. (B) Measured inductances (solid lines) and Q factors (symbol lines) versus operation frequency for a series of tube inductors with 15 coiled turns but different number of strips (2, 4, and 6). (C) Family of curves of inductance as a function of coiled turns for tube inductors with different number of strips (2, 4 and 6) with $W_s = 20 \mu\text{m}$. The open symbols are experimental data, and solid curves are modeled data. (D) Experimental Q_{max} and $f_{Q_{\text{max}}}$ of tube inductors with various configurations on three different substrates, plotted versus the corresponding inductance values. The dashed lines represent the linear fit of each data set obtained from respective substrates.

Q factors for the 4-strip/15-turn device can be found in Fig. S10, where the inductance values are exactly the same on all substrates. In the Fig. 2D, for all substrates, Q_{max} and $f_{Q_{\text{max}}}$ decrease with the inductance, and the slopes of the decrease (the slopes of the linear fittings) vary with substrate conductivities, especially, sapphire showing the slowest degradation, as expected. For the two doped silicon substrates studied, the linear fits of Q_{max} and $f_{Q_{\text{max}}}$ show almost the same slopes and near identical values for the entire inductance range, from 0.4 to 3.5 nH. Their deviations from the sapphire curve become larger with increasing inductance; however, the substrate effect is much less severe for the tube inductors compared to planar counterparts. As an example, in Fig. 2D at the 3.5 nH, the maximum degradation of Q_{max} is only 30% and $f_{Q_{\text{max}}}$ degradation is 50%; in contrast to 150% degradation of Q_{max} at 3.5 nH and 100% degradation of $f_{Q_{\text{max}}}$ at 5 nH for planar spiral inductors²⁶. It is notable that, to achieve the same inductance values and with comparable Q factors, the $f_{Q_{\text{max}}}$ of tube inductors are much higher than that of planar inductors on the same substrates, including doped substrates with low resistivity. For example, at 2.1 nH, on a sapphire substrate, $f_{Q_{\text{max}}}$ increased from 5.6 GHz (planar inductor²⁶) to 23 GHz (tube inductor); and on the $\rho = 10 \Omega\cdot\text{cm}$ p-Si substrate, $f_{Q_{\text{max}}}$ improved from 3.5 GHz (planar inductor²⁶) to 19 GHz for the tube inductor.

In brief, compared to its planar counterpart, the tube inductors demonstrate the excellent substrate immunity and high frequency performance, which can be attributed to its extremely small on-chip footprint and much better confinement of EM field to prevent dissipation to the lossy substrate.

For a comprehensive overview of all the metrics discussed, Fig. 3 benchmarks the footprint and RF performance of 3D tube inductors, inductance L , Q_{max} , $f_{Q_{\text{max}}}$ and footprint, with the state-of-the-art planar spiral inductors used in the $0.18 \mu\text{m}^2$ and 32 nm node²⁷ CMOS technology, where much thicker metal layers (1 μm Al and 4.5 μm Cu, respectively) are used. Clearly, for the same inductance values achieved, the corresponding $f_{Q_{\text{max}}}$ is much higher than that of planar inductors on substrates with similar resistivity. Most remarkably, the rolled-up inductors only occupy 1–10% or less of the on-chip area in comparison. Clearly, once the strained thin film is rolled-up, there are voids left behind on the top of sample which does not reduce the overall footprint at the top level layout. One approach to realize high density assembly and integration of rolled-up passive devices is via the transfer printing process, which can extract the rolled-up tube from the native substrates and transfer to a receiving substrate in desired pattern and density. Preliminary success of transferring the S-RUM tube array off their native substrates has

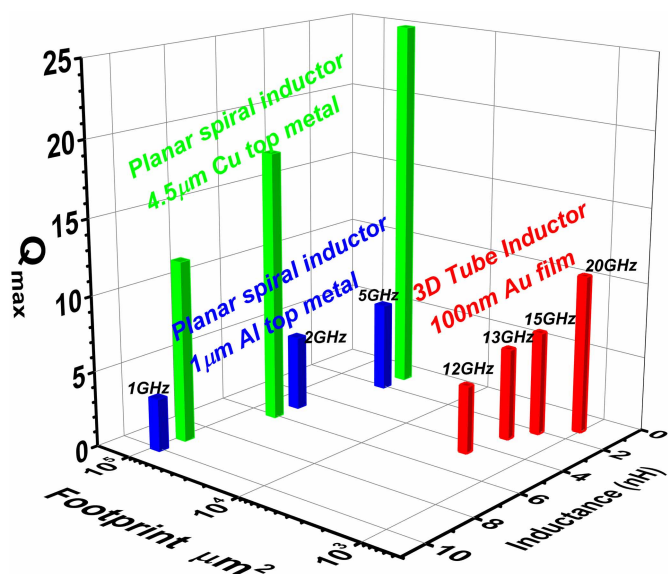


Figure 3 | Benchmark 3D plot. Inductance, footprint, and Q_{max} of rolled-up 3D tube inductors (represented by red pillars) are plotted together with those for planar spiral inductors used in the 0.18 μm and 32 nm node CMOS technology, with 1 μm thick Al (blue pillars) and 4.5 μm thick Cu (green pillars) as the top metal layers, respectively, as indicated. The substrate resistivity is $\rho = 1 \sim 5 \Omega\text{-cm}$ p -type for red and blue pillars and $\rho = 10 \Omega\text{-cm}$ p -type for the green pillars. The marked frequencies correspond to $f_{Q_{max}}$ of the inductors.

already been demonstrated previously¹⁴ and further development is underway. On the other hand, by rolling up the inductors, most of the silicon substrate area could potentially be saved for CMOS devices, resulting in a compact circuit layout. This is in contrast to the circuit layout with planar spiral inductors, where the close proximity of inductors and active devices is not possible because of the strong unwanted EM field coupling between them.

In conclusion, we have successfully demonstrated on-chip self-rolled-up 3D tube inductors. This is achieved by unidirectional S-RUM nanofabrication technique, employing the build-in stress in the SiN_x bilayer integrated with 2D patterned ultra-thin metal strips. The rolled-up tube inductors have shown record inductance/area density, due to the strong mutual coupling effect, which enables an extremely small footprint while maintaining the same inductance. The strong confinement of electromagnetic field within the tube prevents it from dissipating into the substrate. As a result, even on heavily doped silicon substrates, all devices show high self-resonant frequencies, beyond the range achievable by any reported planar or quasi-3D counterparts of the same inductance, highlighting the unprecedented immunity to substrate. By replacing Au with lower resistivity metal such as Cu, Ag, and possibly graphene, Q factors can be increased to be suitable for high performance RFICs. This work establishes S-RUM as a new paradigm that processes like 2D and functions like 3D for other 3D miniaturized functional devices. The ability to control the size, pitch, and orientation in plane, as well as vertical stacking, will enable more complex circuit designs simply using conventional optical lithography. In particular, S-RUM passive electronics can lead to a new kind of RFICs that is ultra-small, light, and highly integratable for applications in portable and wearable electronics in high frequency band.

Methods

To fabricate the 3D rolled-up tube inductor (figure. S1), a 1 μm thick silicon dioxide (SiO_2) was grown by wet thermal oxidation to electrically insulate from the p -type silicon (p -Si) substrate (Note 1 μm thick PECVD SiO_2 was deposited on the sapphire). On the SiO_2 , a 20 nm Germanium (Ge) sacrificial layer was deposited by electron beam evaporation, and it helps to fix and retain the residual stress of all strain

layers. The rectangular mesas were defined by optical lithography and reactive ion etching (RIE). Subsequently, the 60 nm strained SiN_x bilayer was deposited by dual-frequency plasma enhanced chemical vapor deposition (PECVD) to cover the entire sample, which is composed by a 30 nm 380 K low frequency (LF) SiN_x and a 30 nm 13.56 MHz high frequency (HF) SiN_x . Technically, during the deposition, LF RF power induces a compressive strain into the SiN_x thin film, which can be attributed to the excess Si atoms embedded into Si-N and Si-H bonds of SiN_x by bombardment effect. On the other hand, the HF RF power introduces a tensile strain into the SiN_x membrane because of fewer Si atoms and lower density compared to standard stoichiometric ratio Si_3N_4 (S1). In our case, the residual stress of LF and HF SiN_x thin film are -900 MPa and $+300$ MPa, respectively. Then, the 100 nm gold (Au)/5 nm nickel (Ni) serpentine metal lines are deposited on SiN_x bilayer by electron beam evaporation and metal lift-off technology, with $+300$ MPa and $+600$ MPa residual stresses, respectively, a deep trench at one side of mesa is defined by optical lithography and RIE, which is down through to SiO_2 layer. At last, the sample undergoes a wet etching in hydrogen peroxide at 90°C .

- Park, M., Lee, S., Kim, C. S., Yu, H. K. & Nam, K. S. The detailed analysis of high Q CMOS-compatible microwave spiral inductors in silicon technology. *IEEE T. Electron Dev.* **45**, 1953–1959 (1998).
- Yue, C. P. & Wong, S. S. Physical modeling of spiral inductors on silicon. *IEEE T. Electron Dev.* **47**, 560–568 (2000).
- Jiang, H., Wang, Y., Yeh, J. L. & Tien, N. C. On-chip spiral inductors suspended over deep copper-lined cavities. *IEEE T. Microw. Theory* **48**, 2415–2423 (2000).
- Zou, J. *et al.* Development of three-dimensional inductors using plastic deformation magnetic assembly (PDMA). *IEEE T. Microw. Theory* **51**, 1067–1075 (2003).
- Yoon, J. B., Choi, Y. S., Kim, B. I., Eo, Y. & Yoon, E. CMOS-compatible surface-micromachined suspended-spiral inductors for multi-GHz silicon RF ICs. *IEEE Electr. Device L.* **23**, 591–593 (2002).
- Nam, C. M. & Kwon, Y. S. High-performance planar inductor on thick oxidized porous silicon (OPS) substrate. *IEEE Microw. Guided W.* **7**, 236–238 (1997).
- Kim, H. S., Zheng, D., Becker, A. & Xie, Y. H. Spiral inductors on Si p/p/sup+/ substrates with resonant frequency of 20 GHz. *IEEE Electr. Device L.* **22**, 275–277 (2001).
- Tang, C. C., Wu, C. H. & Liu, S. I. Miniature 3-D inductors in standard CMOS process. *IEEE J. Solid-St. Circ.* **37**, 471–480 (2002).
- Park, P., Kim, C. S., Park, M. Y., Kim, S. D. & Yu, H. K. Variable inductance multilayer inductor with MOSFET switch control. *IEEE Electr. Device L.* **25**, 144–146 (2004).
- Yin, W. Y. *et al.* Vertical topologies of miniature multispiral stacked inductors. *IEEE T. Microw. Theory* **56**, 475–486 (2008).
- Prinz, V. Y. *et al.* Free-standing and overgrown InGaAs/GaAs nanotubes, nanohelices and their arrays. *Physica E.* **6**, 828–831 (2000).
- Schmidt, O. G. & Eberl, K. Nanotechnology: Thin solid films roll up into nanotubes. *Nature* **410**, 168–168 (2001).
- Mi, Z. & Bianucci, P. When self-organized In(Ga)As/GaAs quantum dot heterostructures roll up: Emerging devices and applications. *Curr. Opin. Solid. St. M.* **16**, 52–58 (2012).
- Li, X. Strain induced semiconductor nanotubes: from formation process to device applications. *J. Phys. D Appl. Phys.* **41**, 193001 (2008).
- Li, X. Self-rolled-up microtube ring resonators: a review of geometrical and resonant properties. *Adv. Opt. Photonics* **3**, 366–387 (2011).
- Chun, I. S., Challa, A., Derickson, B., Hsia, K. J. & Li, X. Geometry effect on the strain-induced self-rolling of semiconductor membranes. *Nano Lett.* **10**, 3927–3932 (2010).
- Mei, Y. *et al.* Versatile approach for integrative and functionalized tubes by strain engineering of nanomembranes on polymers. *Adv. Mater.* **20**, 4085–4090 (2008).
- Rottler, A. *et al.* Rolled-up nanotechnology for the fabrication of three-dimensional fishnet-type GaAs-metal metamaterials with negative refractive index at near-infrared frequencies. *Appl. Phys. Lett.* **100**, 151104 (2012).
- Pizzi, M., Koniachkine, V., Nieri, M., Sinesi, S. & Perlo, P. Electrostatically driven film light modulators for display applications. *Microsyst. Technol.* **10**, 17–21 (2003).
- Huang, M. *et al.* Nanomechanical Architecture of Strained Bilayer Thin Films: From Design Principles to Experimental Fabrication. *Adv. Mater.* **17**, 2860–2864 (2005).
- Deneke, C., Müller, C., Jin-Phillipp, N. Y. & Schmidt, O. G. Diameter scalability of rolled-up In(Ga)As/GaAs nanotubes. *Semicond. Sci. Tech.* **17**, 1278 (2002).
- Vaccaro, P. O., Kubota, K. & Aida, T. Strain-driven self-positioning of micromachined structures. *Appl. Phys. Lett.* **78**, 2852–2854 (2001).
- Froeter, P. *et al.* 3D hierarchical architectures based on self-rolled-up silicon nitride membranes. *Nanotechnology* **24**, 475301 (2013).
- Burghartz, J. N. & Rejaei, B. On the design of RF spiral inductors on silicon. *IEEE T. Electron Dev.* **50**, 718–729 (2003).
- Huang, W. *et al.* On-Chip Inductors with Self-Rolled-Up SiN_x Nanomembrane Tubes: A Novel Design Platform for Extreme Miniaturization. *Nano Lett.* **12**, 6283–6288 (2012).
- Burghartz, J. N. *et al.* Monolithic Spiral Inductors Fabricated Using a VLSI Cu-Damascene Interconnect Technology and Low-Loss Substrates. *Int. El. Devices*



- Meet.* 99–102. San Francisco, CA, USA. IEEE. DOI:10.1109/IEDM.1996.553131 (1996).
27. Jan, C. H. *et al.* RF CMOS technology scaling in High-k/metal gate era for RF SoC (system-on-chip) applications. *Int. El. Devices Meet.* 27.2.1–27.2.4. San Francisco, CA, USA. IEEE. DOI:10.1109/IEDM.2010.5703431 (2010).

Acknowledgments

Financial support was provided in part by DARPA # N66001-13-1-4031 (X.Y., X.L.) and NSF ECCS # 1309375 (W.H., M.L., X.L.).

Author contributions

X.Y. designed, performed experiments and data analysis. W.H. and M.L. assisted in design and data analysis. T.C., S.G. and J.S. assisted in data analysis. X.L. supervised the project. All authors contributed to the writing of the manuscript.

Additional information

Supplementary information accompanies this paper at <http://www.nature.com/scientificreports>

Competing financial interests: The authors declare no competing financial interests.

How to cite this article: Yu, X. *et al.* Ultra-Small, High-Frequency, and Substrate-Immune Microtube Inductors Transformed from 2D to 3D. *Sci. Rep.* 5, 9661; DOI:10.1038/srep09661 (2015).



This work is licensed under a Creative Commons Attribution 4.0 International License. The images or other third party material in this article are included in the article's Creative Commons license, unless indicated otherwise in the credit line; if the material is not included under the Creative Commons license, users will need to obtain permission from the license holder in order to reproduce the material. To view a copy of this license, visit <http://creativecommons.org/licenses/by/4.0/>